Nanoscale

PAPER

View Article Online
View Journal | View Issue

Cite this: *Nanoscale*, 2024, **16**, 3583

A thiolated copper-hydride nanocluster with chloride bridging as a catalyst for carbonylative C–N coupling of aryl amines under mild conditions: a combined experimental and theoretical study†

Anish Kumar Das, ‡[a] Sourav Biswas,‡[a] Amit Pal,[a] Surya Sekhar Manna, [b] Avirup Sardar, [a] Pradip Kumar Mondal,[c] Basudev Sahoo, *[a] Biswarup Pathak *[b] and Sukhendu Mandal *[a]

Atomically precise copper nanoclusters (Cu NCs), an emerging class of nanomaterials, have garnered significant attention owing to their versatile core–shell architecture and their potential applications in catalytic reactions. In this study, we present a straightforward synthesis strategy for $[Cu_{29}(S^tBu)_{12}(PPh_3)_4Cl_6H_{10}][BF_4]$ (Cu_{29}) NCs and explore their catalytic activity in the carbonylative C–N coupling reaction involving aromatic amines and N-heteroarenes with dialkyl azodicarboxylates. Through a combination of experimental investigations and density functional theory studies, we elucidate the radical mechanisms at play. The crucial step in the catalytic process is identified as the decomposition of diisopropyl azodicarboxylates on the surface of Cu_{29} NCs, leading to the generation of oxyacyl radicals and the liberation of nitrogen gas. Subsequently, an oxyacyl radical abstracts a hydrogen atom from aniline, initiating the formation of an aminyl radical. Finally, the aminyl radical reacts with another oxyacyl radical, culminating in the synthesis of the desired carbamate product. This detailed analysis provides insights into the intricate catalytic pathways of Cu_{29} NCs, shedding light on their potential for catalyzing carbonylative C–N coupling reactions.

Received 21st November 2023,
Accepted 8th January 2024

DOI: 10.1039/d3nr05912j

rsc.li/nanoscale

Introduction

Since the discovery of nanoclusters (NCs), gold (Au) and silver (Ag) NCs have emerged due to their relatively superior stability compared to the lighter congeners of transition elements.[1–3] However, the progressing research interest has now developed strategies to synthesize copper (Cu) NCs, the most abundant and lightest congener of group 11.[4–11] Discrete molecular properties and quantum confinement make these NCs more promising for applications than their nanoparticle counterparts.[2,12] In addition to this, their precise structural architecture, high surface-to-volume ratio, low half-cell reduction potential, and high chemical reactivity appear advantageous for opening up their unique opportunities in catalytic activity.[13–17] Generally, metal NCs consist of a core architecture of metal atoms surrounded by metal-ligand motifs. The interconnectivity between metals and ligands creates a different core configuration that preferentially governs the geometric architecture of the overall NCs and creates active catalytic sites with fewer coordination bonds, which are inaccessible in any other contemporary materials.[18–24]

The history of CuH complexes dates back to the early 1800s when they were first discovered.[25,26] Initially, their application was primarily focused on catalytic reactions involving the reduction of intermediates.[27] However, it took several more decades for these complexes to find their applications as catalysts in organic media. A significant turning point in the utilization of Cu in catalysis occurred with the discovery of organocopper species, famously known as Stryker's reagent.[28,29] This breakthrough expanded the range of applications for copper-based materials, enabling the construction of useful chemical bonds beyond their purely reductive capabilities. From that moment on, organocopper species garnered significant attention in the scientific community due to copper's economic advantages as a catalyst. Researchers recognized the potential

[a]*School of Chemistry, Indian Institute of Science Education and Research Thiruvananthapuram, Kerala 695551, India. E-mail: sukhendu@iisertvm.ac.in, basudev@iisertvm.ac.in*
[b]*Department of Chemistry, Indian Institute of Technology Indore, Madhya Pradesh 453552, India. E-mail: biswarup@iiti.ac.in*
[c]*Elettra Sincrotrone Trieste, Area Science Park, 341494 Basovizza, Italy*

†Electronic supplementary information (ESI) available. CCDC 2242226. For ESI and crystallographic data in CIF or other electronic format see DOI: https://doi.org/10.1039/d3nr05912j

‡These authors contributed equally to this work.

of copper as a superior catalyst, which spurred further exploration and experimentation. The development of Cu NC-based catalysts has a pronounced effect on this field. There are few studies now available in the literature where Cu NCs have already been utilized in various catalytic reactions; however, the examples are still limited and in most of the cases, the mechanism of the catalyst is not properly explored.[16,20,30–32] Thus, it would be useful if a precise structural architecture could be developed in such a way that it overcomes the challenges associated with the thiolate Cu NCs to be utilized as an active catalyst.

Carbon–nitrogen (C–N) bonds are pervasive in natural products, agrochemicals, and pharmaceutical compounds, underscoring their immense importance.[33,34] Recognizing the significance of C–N bonds, there is a growing emphasis on designing effective catalysts in synthetic chemistry to facilitate the convenient formation of these bonds.[35] Traditionally, Cu catalysts, coordinated with ligands, have been the primary choice for such reactions. One illustrative example of this is the synthesis of organic carbamates through carbonylation, where N–H bond cleavage and C–N bond formation occur simultaneously under the influence of Cu catalysts at elevated temperatures and with the use of various toxic chemicals.[36,37] Over time, several approaches have been explored, including the substitution of Cu with other transition metal atoms. However, the ultimate objective of synthesizing carbamates through simpler and more convenient methods has remained elusive. Hence, the quest for alternative methods remains a desirable pursuit. In this context, a noteworthy development by Usman *et al.* involves the use of dialkyl azodicarboxylates as the carbonyl source in the carbonylation of aniline.[38] This innovative approach employs the $Cu(OAc)_2$ salt as a catalyst, and notably, the reaction occurs at room temperature, offering a promising alternative for the synthesis of carbamates. However, the use of dialkyl azodicarboxylates in copper-catalyzed carbonylation reactions is still limited.[39] While homogeneous M–H-based molecular catalysts have made strides in organic synthesis, the potential of emerging M–H-based metal NCs as homogeneous catalysts in organic reactions has yet to be fully explored. Recently, Lee *et al.* have reported the synthesis of a Cu_{32} NC that exhibited catalytic effectiveness in a carbonylation reaction of aniline using diisopropyl azodicarboxylate, albeit with a limited substrate scope.[15] However, the influence of the precise structural architecture of the Cu_{32} NC on this specific reaction remains unknown.

Based on the aforementioned facts, a one-pot synthesis strategy is presented for producing a $[Cu_{29}(S^tBu)_{12}(PPh_3)_4Cl_6H_{10}][BF_4]$ (Cu_{29}) NC with a core–shell architecture. This precise core–shell configuration not only imparts an appealing structure but also exerts an influence on the optical and catalytic properties. The computational investigation constructs the electronic structure of the as-synthesized Cu_{29} NC where it is found that the occupied orbitals are mostly contributed by the metal–ligand motif shell; however, the unoccupied orbitals are predominantly contributed by the inner core. Due to this unique arrangement, this NC can take part efficiently in the carbonylation reaction. The efficiency under milder conditions makes it highly valuable for C–N bond-forming reactions due to the precise availability of the active catalytic sites which stabilize the radical intermediates.

Results and discussion

In a typical synthesis of Cu NCs, a Cu(I) salt, *i.e.*, $Cu(CH_3CN)_4BF_4$ in acetonitrile/chloroform 4 : 1 (v/v) was treated with HS^tBu and PPh_3, followed by the addition of methanolic $NaBH_4$ solution at room temperature (Fig. 1a). After a visible color change, the resulting orange precipitate was purified, dissolved in a chloroform/hexane mixture, and left to crystallize under ambient conditions. After seven days, we obtained red-colored, plate-like single crystals, as confirmed by microscopic imaging (Fig. S1†). The resulting structure crystallized in a triclinic crystal system with the space group $P\bar{1}$ (no. 2) (Table S1†). Its overall morphology is tetrahedral, consisting of 29 Cu atoms protected by 12 $-S^tBu$, 6 Cl^-, 10 hydrides, and 4 PPh_3 ligands (Fig. 1b). Single-crystal X-ray diffraction analysis also revealed the presence of one BF_4^- ion and uncoordinated $CHCl_3$ in the lattice per formula unit. The origin of the Cl^- ions in the structure can be attributed to the cleavage of carbon–chlorine (C–Cl) bonds in $CHCl_3$ during the reaction process. Additionally, the presence of hydrides in the structure can be traced back to the addition of sodium borohydride ($NaBH_4$). This observation is substantiated by analyzing ^1H NMR peaks of the as-synthesized deuteride analogue ($Cu_{29}D$ NC) of Cu_{29} NC under similar reaction conditions using $NaBD_4$. The ^1H NMR spectrum of the Cu_{29} NC distinctly shows hydride peaks ranging from 3.7 to 1.9 ppm (Fig. S2†). The deshielding order of these bridged hydrides aligns with our structural classification, as detailed in Table S2.† However, the absence of these hydride peaks in the $Cu_{29}D$ NC spectrum, together with the unchanged appearance of other peaks, indicates the complete replacement of all ten hydrides in the Cu_{29} NC with deuterium (Fig. S3†). The presence of respective elements is further confirmed through ^{11}B, ^{19}F, and ^{31}P NMR measurements (Fig. S4–S6†).

The Cu_{29} NC exhibits a core–shell architecture, wherein a central Cu-centered Cu_{12} ($Cu@Cu_{12}$) core is protected by a $Cu_{16}S_{12}P_4Cl_6$ metal–ligand motif shell (Fig. 1c and d). This structural architecture was previously reported by Sun *et al.*[40] In contrast to another reported Cu_{29} NC (Cu_{29}-Adm NC) with adamantane thiolate (–SAdm), we observe a difference in the connecting chlorides (Fig. S7†).[41] This discrepancy in chloride connections is a critical factor that contributes to the structural disparity between these two scenarios.

The existing literature has established a correlation between the incorporation of chloride ligands onto the motif shell and the steric properties of the thiolate ligands utilized in the synthesis.[41] However, in our specific case, a noteworthy observation emerges. Despite using a less bulky thiolate ligand ($-S^tBu$) in comparison with the adamantane thiolate used in previous studies, we have encountered a higher number of chloride ligands within the metal–ligand motif shell. This intriguing finding indicates that steric effects alone do not

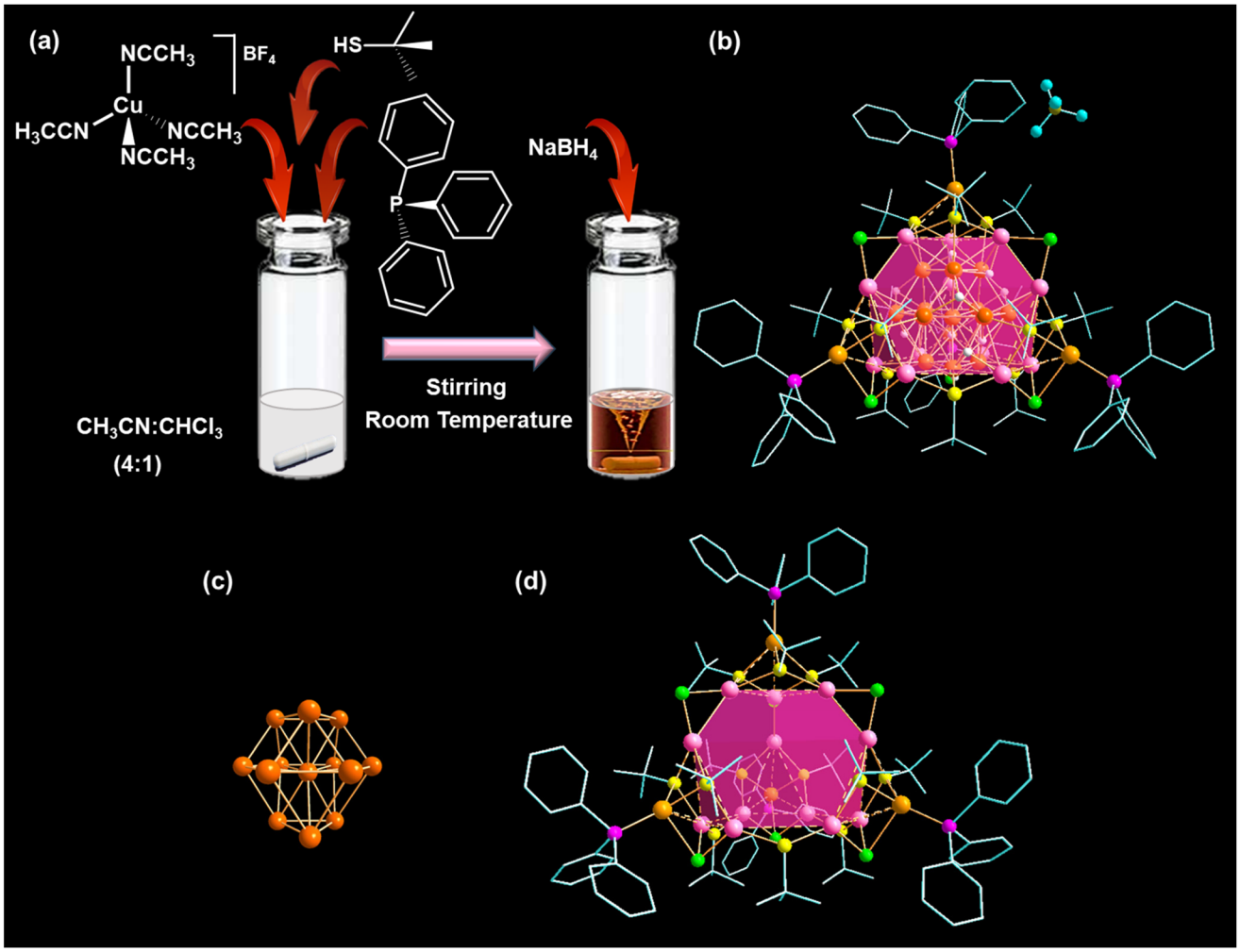

Fig. 1 (a) Reaction scheme for the synthesis of the Cu_{29} NC, (b) obtained crystal structure, (c) distorted triangular orthobicupola-like geometry of the Cu@Cu_{12} core, and (d) the metal–ligand motif shell of the Cu_{29} NC. Color legend: Cu(core), deep orange; Cu(Cu_{12} shell), rose; Cu(Cu_4 shell), light orange; S, yellow; P, magenta; Cl, green; C, grey stick; B, dark yellow; F, turquoise; H, white. H atoms and solvent molecules are partially omitted for clarity.

determine the addition of smaller ligands to the motifs. To accommodate a greater quantity of these smaller ligands on the outer surface, we intentionally altered the polarity of the reaction mixture. Notably, whereas Bao *et al.* previously employed a tertiary solvent mixture initially composed of acetonitrile and chloroform in a 1 : 1 (v/v) ratio, followed by the addition of methanol, our approach utilized a 4 : 1 (v/v) mixture of acetonitrile and chloroform initially, followed by the addition of methanol.[41] This deliberate adjustment in solvent polarity, favouring a higher polar nature, accentuated the addition of chloride ligands. Consequently, it resulted in the formation of the metal–ligand motif shell with a reduced number of thiolate ligands. Therefore, it becomes evident that solvent polarity might play a role in shaping the intricate structure of Cu NCs, further emphasizing the multifaceted factors influencing their composition and morphology.

A positive mode ESI-MS measurement was performed by dissolving the as-synthesized NC in a $CHCl_3$ and methanol mixture (v/v ~1 : 1) resulting in a single molecular ion at m/z = 4185.04 with no cluster fragmentation signal, indicating its structural stability (Fig. S8a†). The isotopic distribution of the obtained peak shows its mono-cationic nature and the peak is assigned to the formula $[Cu_{29}(S^tBu)_{12}(PPh_3)_4Cl_6H_{10}]^+$, which matches the simulated m/z value of 4184.93. The good agreement between experimental and simulated isotopic patterns confirmed its complete molecular formula (inset; Fig. S8a†). However, hydride identification by crystallographic techniques is notoriously challenging due to its low electron density compared to other elements present in the structure. Here, the complete formula of the NC was determined as $[Cu_{29}(S^tBu)_{12}(PPh_3)_4Cl_6H_{10}][BF_4]$, combining SCXRD and ESI-MS data. Additionally, the ESI-MS measurement of the deuteride analogue $[Cu_{29}(S^tBu)_{12}(PPh_3)_4Cl_6D_{10}]^+$ confirmed the presence of ten hydrides in the NC, as evidenced by a distinct peak at m/z 4195.12 (Fig. S8b†). The valence state and composition of the Cu_{29} NC were further characterized by XPS and

EDS analyses (Fig. S9 and S10†). Peaks corresponding to Cu $2p_{3/2}$ and Cu $2p_{1/2}$ are observed in the binding energy spectrum of Cu 2p at 931.38 eV and 951.25 eV, respectively (Fig. S11†). The doublet separation is found to be 19.87 eV, and the dominant peak in the Cu LMM Auger spectrum is noticed at 916.3 eV, justifying the +1 oxidation state of all Cu (Fig. S12†). Consequently, it further verifies the obtained crystal structure of the Cu_{29} NC, where the mono-catatonic nature of the Cu_{29} NC was identified.

The as-synthesized Cu_{29} NC in $CHCl_3$ exhibits absorbance peaks at 325, 445, and 527 nm in the UV-vis absorption spectrum (Fig. 2a). These peaks align well with the simulated absorption spectrum obtained through TD-DFT calculations. The highest oscillator strength peaks at 326, 437, and 517 nm correspond to specific transitions: HOMO−10 → LUMO+2, HOMO−8 → LUMO, and HOMO−2 → LUMO, respectively (Fig. 2b and c). These slight deviations can be attributed to the ligand simplifications employed in the theoretical calculations. The Kohn–Sham diagram reveals that the occupied orbitals primarily involve s and p-like states of the ligand and s, p, and d-like states of the Cu atoms in the shell, while the unoccupied orbitals mainly consist of s, p, and d-like states of the Cu atoms in the core. The presence of discernible peaks in the absorption spectrum suggests that these peaks originate from charge transitions occurring between the metal–ligand shell and the inner core of the Cu_{29} NC. Consequently, any alteration in the architecture of the ligand shell will inevitably influence the dynamics of these charge transition processes. This phenomenon becomes evident when we compare our UV-vis absorbance results with the reported literature concerning Cu_{29} NCs featuring $Cu_{16}S_{18}P_4$ and $Cu_{16}S_{15}P_4Cl_3$ motif shells.[41] So, the introduction of chloride ions into the ligand shell is likely to induce changes in the electronic environment of the ligand shell itself. These alterations have a profound impact on the charge transition process, which is apparent from the discrepancies observed in the UV-vis absorption spectrum. This underscores that the sensitivity of the absorption spectrum depends on the ligand shell architecture. Moreover, the absorption spectra of the as-synthesized NC remain largely unchanged even after exposure to the ambient atmosphere for 7 days and sunlight for 4 hours, demonstrating its excellent resistance to photodegradation (Fig. S13†). This structural stability can be attributed to the distinctive structural architecture of the Cu_{29} NC.[42]

Encouraged by the unique characteristics, including the precise atomic structures, exact molecular formula and inherent stability of emerging copper nanoclusters, we wondered if the as-synthesized Cu_{29} NC would be catalytically active to promote the organic transformations, despite the presence of a sulfur-containing ligand at the outer surface of the NC. We commenced our study by reacting aniline (**1a**) with diisopropyl azodicarboxylate (**2a**) in the presence of Cu_{29} NCs

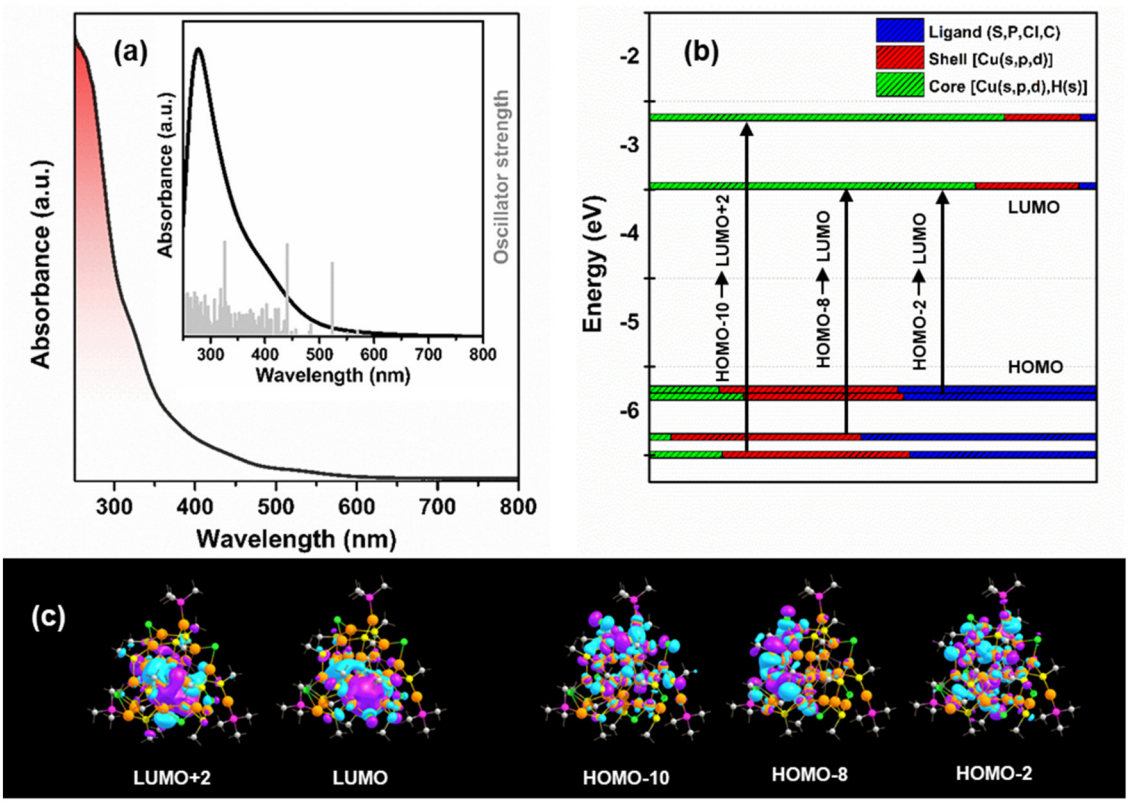

Fig. 2 (a) UV-vis absorption spectrum of the as-synthesized Cu_{29} NC in $CHCl_3$; the inset shows the simulated absorption spectrum with oscillator strength, (b) Kohn–Sham diagram and the associated transitions, and (c) FMOs of the associated energy states. Color legend: Cu, orange; S, yellow; P, magenta; Cl, green; C, grey.

(0.25 mol% Cu) in $CDCl_3$ solvent at room temperature for 3 h, furnishing the desired carbamate product **3aa** in a good yield (Fig. 3). The control experiments conducted in the absence of Cu_{29} NCs or even in the presence of a CuI salt, in lieu of Cu_{29} NCs, resulted in no **3aa** product formation or its formation in traces (Fig. 3). In addition to that, we have performed the controlled reaction of **3aa** product formation in the presence of another Cu(I) salt, $Cu(CH_3CN)_4BF_4$ as a catalyst, which is a precursor salt of the synthesis of the as-synthesized Cu_{29} NC, resulting in the formation of product **3aa** in a trace amount (<5%) (Fig. 3). Furthermore, we explored the same catalytic reaction using an *in situ* mixture of $Cu(CH_3CN)_4BF_4$, HS-^{t}Bu,

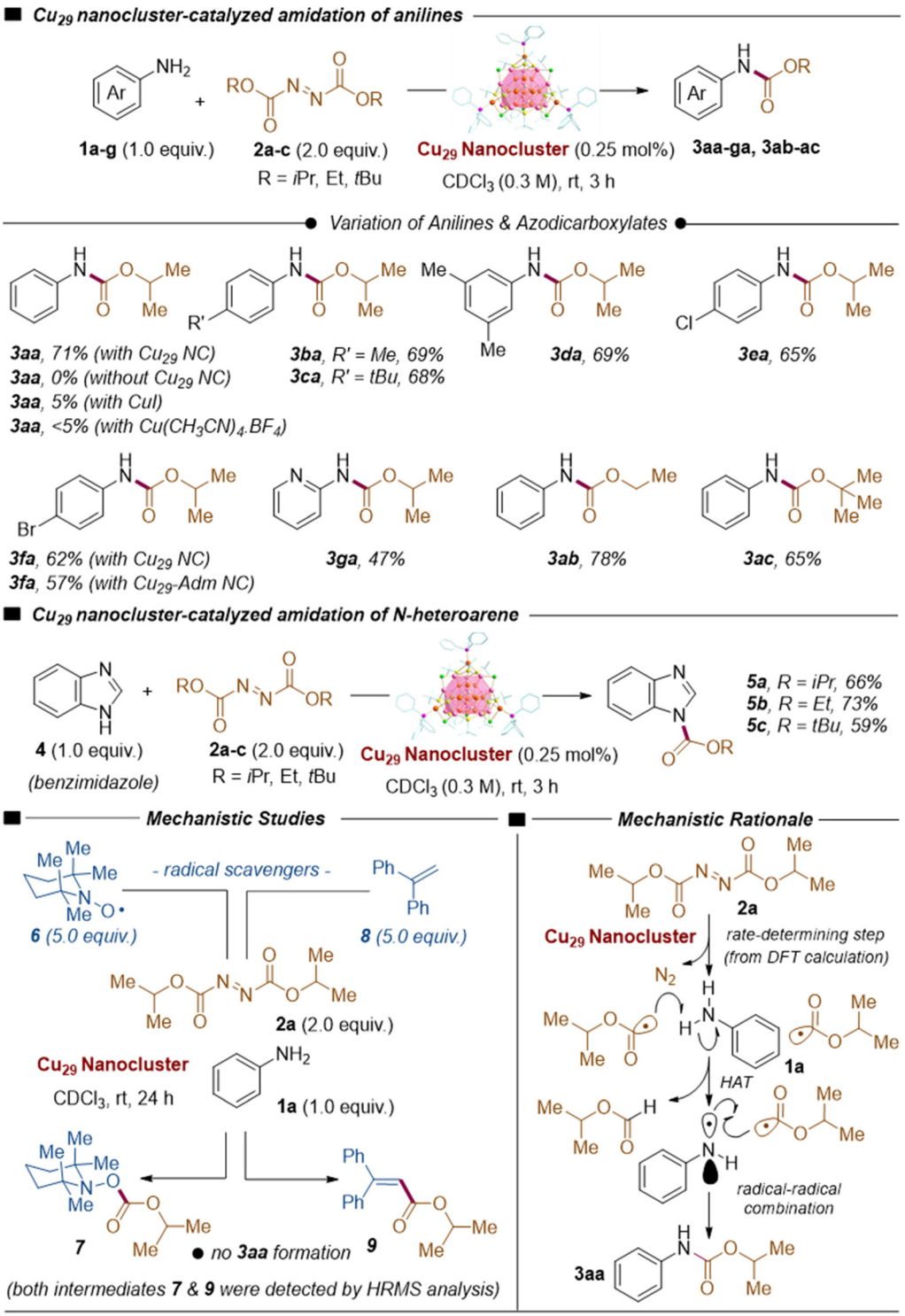

Fig. 3 Cu_{29} NC-catalyzed carbamate synthesis from anilines and benzimidazole, mechanistic studies, and mechanistic rationale.

PPh_3, and $NaBH_4$ as the catalyst precursor. Notably, the yield decreased to 11%. This reduction in yield may be attributed to the potential interference from organic ligands and reducing agents with the product. It is indicative of an imperative role of the Cu_{29} NC in this catalytic transformation. The synthetic utility of Cu_{29} NC-catalyzed C–N coupling was evaluated by employing a plethora of distinctly substituted anilines and a variety of dialkyl azodicarboxylates under standard reaction conditions. Gratifyingly, the electron-rich *p*-methyl and *p-tert*-butyl anilines (**1b** and **1c**) reacted well with diisopropyl azodicarboxylate (**2a**) in this transformation, delivering the carbamate products **3ba** (69%) and **3ca** (68%), respectively, in good yields. Furthermore, 3,5-dimethylaniline (**1d**) also provided the desired product **3da** (69%) in a good yield. Moreover, the electron-poor *p*-chloro- and *p*-bromoanilines (**1e** and **1f**) remained as viable substrates, affording carbamates **3ea** (65%) and **3fa** (62%), respectively. Notably, heteroaryl 2-aminopyridine (**1g**) was also a competent reaction partner, furnishing product **3ga** (47%) in a moderate yield. Delightfully, this method was extendable to different dialkyl azodicarboxylates, such as diethyl azodicarboxylate (**2b**) and di-*tert*-butyl azodicarboxylate (**2c**), delivering carbamates **3ab** (78%) and **3ac** (65%), respectively, in good yields. Nevertheless, the success of various anilines prompted us to further explore the catalytic activity of the Cu_{29} NC in the C–N coupling of the benzimidazole N–H bond with dialkyl azodicarboxylates. Indeed, the dialkyl azodicarboxylates (**2a–2c**) exhibited viability in this transformation, while they were treated with benzimidazole (**4**), offering the carbamate products **5a–5c** (66%, 73%, and 59%, respectively) in good yields. In a comparative study, our Cu_{29} NC catalyst exhibited superior catalytic activity compared to a previously reported Cu_{32} NC catalyst for carbonylative C–N bond formation. Following the identical catalytic procedure reported in the literature, the Cu_{29} catalyst achieved an impressive yield of 59% for the synthesis of **3fa**, surpassing the reported yield of 46.7% using the Cu_{32} catalyst. This significant increase in yield highlights the superior efficiency of the Cu_{29} catalyst, solidifying its potential as a highly efficient homogeneous catalyst for carbonylative C–N bond formation reactions.

To shed light on the mechanistic scenario, radical inhibition experiments were conducted in the presence of radical scavengers. An adduct (**7**) of the so-formed oxyacyl radical and TEMPO (**6**) was detected by high-resolution mass spectrometric (HRMS) analysis when the standard reaction was executed in the presence of TEMPO (**6**) (TEMPO = (2,2,6,6-tetramethylpiperidin-1-yl) oxyl) as a radical scavenger. Furthermore, the standard reaction was inhibited by 1,1-diphenylethene (**8**), forming an oxyacyl radical-trapped intermediate (**9**) that was identified by HRMS analysis. These experiments support the involvement of a radical intermediate in the reaction mechanism.

To understand the mechanism more properly, we have plotted the free energy profile diagram which we obtained by theoretical calculations (Fig. 4 and Table S3†). Initially, the addition of diisopropyl azodicarboxylates (Azo) to the reaction medium with the catalyst produces **b** with an exergonic free energy change (−0.74 eV), which could be due to the H-bonding interaction (2.8–3.1 Å) between the Azo and Cl atoms of the Cu_{29} NC. Furthermore, complex **c** with two carbonyl radicals is formed upon two C–N bond cleavage of Azo with a free energy change of 2.58 eV. As the radical generation reaction is too fast, we have considered the concerted pathway. This endergonic reaction might be due to the electronic repulsion between free radicals on carbon atoms and lone pairs of Cl atoms in the Cu_{29} NC. Next, complex **d** is formed in the presence of aniline with a reaction free energy change of −0.61 eV. Complex **e** is formed by C–H bond formation between the carbonyl compound and the aniline radical. A transition state is located in between **d** and **e**, which requires an activation barrier of 0.59 eV. The activated **e** complex undergoes a concerted pathway with the second carbonyl radical and forms a stable C–N complex with a free energy change of −3.7 eV, suggesting a favourable carbamate formation. Hence, the highly exergonic nature of the overall reaction free energy change (−2.95 eV) indicates the thermodynamic favourability of the reaction.

Based on experimental and theoretical studies, a proposed mechanism suggests that in the rate-determining step, diisopropyl azodicarboxylates (**2a**) decompose over Cu_{29} NCs, generating oxyacyl radicals (2 equiv.) with the extrusion of N_2 gas. Hydrogen atom abstraction (HAT) from aniline (**1a**) by the oxyacyl radical generates an aminyl radical, which then combines with another oxyacyl radical to produce the final carbamate product **3aa**. The catalytic activity of the Cu_{29} NC is influenced by its specific structural architecture, including the arrangement of active sites and the surrounding chemical environment, which contribute to achieving the desired catalytic activity for different substrates.

The key stabilizing interaction identified is the H-bonding interaction (2.8–3.1 Å) between the Azo and Cl atoms of the Cu_{29} NC. This underscores the pivotal role of the Cl atom within the catalyst, influencing the entire catalytic reaction pathway. In essence, the presence of a Cl atom on the motif shell emerges as a crucial factor shaping the catalytic properties of the system. The involvement of the Cl atom is central to the enhancement of the catalytic activity of the Cu_{29} NC, particularly when compared to the Cu_{32} and Cu_{29}-Adm NCs, which contain fewer chloride bridges in the motif (Fig. 3). Indeed, the introduction of a higher quantity of Cl atoms into the Cu_{29} NC structure significantly amplifies the number of available catalytic sites. These catalytic sites represent critical locations where chemical transformations and reactions can occur efficiently. This augmentation of catalytic sites is indispensable for the Cu_{29} NC to exhibit and sustain its catalytic activities effectively.

To ensure post-catalytic stability, we conducted several tests. TEM images of the Cu_{29} NC catalyst before and after the **3fa** formation showed consistent cluster size, indicating the stability and uniform distribution of the NC throughout the catalysis reaction (Fig. S14†). Comparable absorption spectra of the catalyst (before and after the catalytic reaction) revealed significant similarity, which also suggests the stability of the NC after the catalytic reaction (Fig. S15†). Additionally, the ESI-MS data of the post-reaction catalyst closely matched those

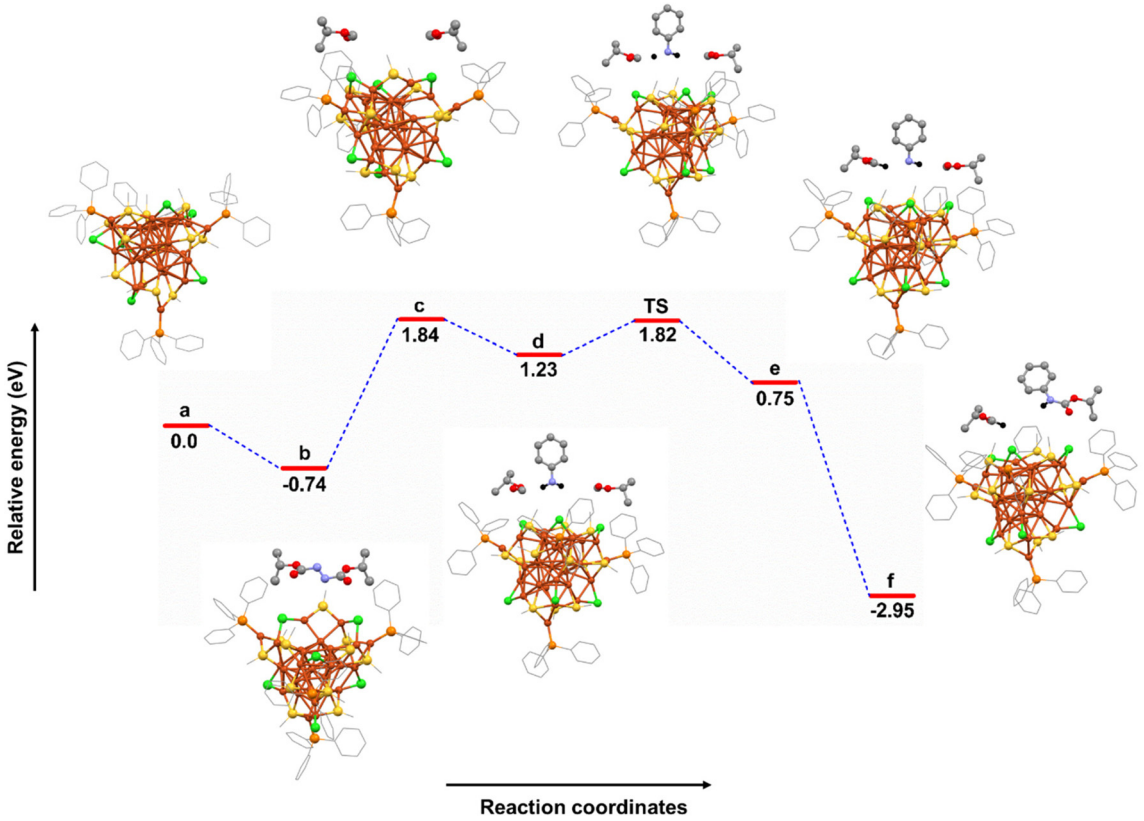

Fig. 4 Mechanistic study of the catalytic reaction from the theoretical investigation. Color legend: Cu, dark orange; S, yellow; P, light orange; Cl, green; N, blue; O, red; C, grey; H, black. H atoms are partially removed for clarity.

of the as-synthesized catalyst, confirming the intact structure and composition (Fig. S16†). ^{1}H NMR measurements of the post-reaction catalyst showed clear matching with the catalyst before the reaction (Fig. S17†). Notably, consistent peak integration in the hydride region confirmed and quantified the presence of hydrides in the isolated catalyst after the reaction.

Conclusions

In conclusion, our study has successfully engineered a core–shell architecture for atomically precise Cu NCs, showcasing their efficacy as homogeneous catalysts in carbonylative C–N coupling reactions. The designed NC exhibits a distinctive geometry, featuring a central Cu@Cu_{12} core intricately enveloped by a $Cu_{16}S_{12}P_4Cl_6$ metal–ligand motif shell, accompanied by ten hydride ligands. We have systematically investigated the impact of this nanocluster on carbonylative C–N coupling reactions involving aromatic amines and heteroaromatic benzimidazole substrates. Remarkably, these transformations occur under mild reaction conditions, yielding a diverse array of carbamates in high yields through a radical-assisted mechanistic pathway. Our innovative synthetic approach, together with comprehensive structural insights, has unveiled the significant role of the Cl atom within the NC structure. This observation holds the potential to inspire further advancements in the synthesis of novel metal nanoclusters with tailored catalytic properties. The implications of our findings extend beyond the specific catalytic system studied here, contributing valuable knowledge to the broader landscape of materials science and catalysis research.

Data availability

The ESI contains experimental details, computational methods, structural refinement parameters, the presence of hydrides in the structure, theoretical insights into the catalysis, SEM micrograph of the as-synthesized crystal, ^{1}H, ^{11}B, ^{19}F, ^{31}P NMR of the Cu_{29} NC, ^{1}H NMR of the Cu_{29}D NC, structural illustration, XPS and EDS spectra of the Cu_{29} NC, stability of the Cu_{29} NC, catalyst characterization after the catalytic reaction, NMR spectra of all products obtained after catalysis, and coordinates of the optimized structure and references.

Author contributions

A. K. D., S. B., and A. S. performed the synthesis, characterization and data interpretation. A. P. and B. S. were involved in the catalysis. P. K. M. solved the crystal structure. S. S. M. and B. P. performed the theoretical calculation. S. M. was involved in manuscript preparation. All authors discussed the results and were involved in manuscript writing.

Conflicts of interest

There are no conflicts to declare.

Acknowledgements

We acknowledge funding from the Science and Engineering Research Board (SERB) through the grants CRG/2022/000984. We are also thankful to Ms Saniya Gratious and Ms Sariga Mangalamundackal Vijayan for their help in ESI-MS measurement and initial synthesis, respectively.

References

1 R. Jin, C. Zeng, M. Zhou and Y. Chen, *Chem. Rev.*, 2016, **116**, 10346–10413.
2 I. Chakraborty and T. Pradeep, *Chem. Rev.*, 2017, **117**, 8208–8271.
3 S. Biswas, S. Das and Y. Negishi, *Coord. Chem. Rev.*, 2023, **492**, 215255.
4 S. Sharma, K. K. Chakrahari, J.-Y. Saillard and C. Liu, *Acc. Chem. Res.*, 2018, **51**, 2475–2483.
5 X. Liu and D. Astruc, *Coord. Chem. Rev.*, 2018, **359**, 112–126.
6 A. Baghdasaryan and T. Bürgi, *Nanoscale*, 2021, **13**, 6283–6340.
7 A. K. Das, S. Biswas, V. S. Wani, A. S. Nair, B. Pathak and S. Mandal, *Chem. Sci.*, 2022, **13**, 7616–7625.
8 S. Biswas, S. Hossian, T. Kosaka, J. Sakai, D. Arima, Y. Niihori, M. Mitsui, D.-e. Jiang, S. Das, S. Wang and Y. Negishi, *Chem. Commun.*, 2023, **59**, 9336–9339.
9 T. Jia, Z.-J. Guan, C. Zhang, X.-Z. Zhu, Y.-X. Chen, Q. Zhang, Y. Yang and D. Sun, *J. Am. Chem. Soc.*, 2023, **145**, 10355–10363.
10 B.-L. Han, Z. Liu, L. Feng, Z. Wang, R. K. Gupta, C. M. Aikens, C.-H. Tung and D. Sun, *J. Am. Chem. Soc.*, 2020, **142**, 5834–5841.
11 R. S. Dhayal, W. E. van Zyl and C. Liu, *Acc. Chem. Res.*, 2016, **49**, 86–95.
12 C. M. Aikens, *Acc. Chem. Res.*, 2018, **51**, 3065–3073.
13 R. S. Dhayal, J.-H. Liao, Y.-R. Lin, P.-K. Liao, S. Kahlal, J.-Y. Saillard and C. Liu, *J. Am. Chem. Soc.*, 2013, **135**, 4704–4707.
14 S. Nematulloev, A. Sagadevan, B. Alamer, A. Shkurenko, R. Huang, J. Yin, C. Dong, P. Yuan, K. E. Yorov and A. A. Karluk, *Angew. Chem., Int. Ed.*, 2023, **62**, e202303572.
15 S. Lee, M. S. Bootharaju, G. Deng, S. Malola, W. Baek, H. Hakkinen, N. Zheng and T. Hyeon, *J. Am. Chem. Soc.*, 2020, **142**, 13974–13981.
16 A. W. Cook, Z. R. Jones, G. Wu, S. L. Scott and T. W. Hayton, *J. Am. Chem. Soc.*, 2018, **140**, 394–400.
17 Y. Du, H. Sheng, D. Astruc and M. Zhu, *Chem. Rev.*, 2019, **120**, 526–622.
18 C. Sun, N. Mammen, S. Kaappa, P. Yuan, G. Deng, C. Zhao, J. Yan, S. Malola, K. Honkala and H. Häkkinen, *ACS Nano*, 2019, **13**, 5975–5986.
19 G.-G. Luo, Z.-H. Pan, B.-L. Han, G.-L. Dong, C.-L. Deng, M. Azam, Y.-W. Tao, J. He, C.-F. Sun and D. Sun, *Angew. Chem., Int. Ed.*, 2023, **62**, e202306849.
20 G. Dong, Z. Pan, B. Han, Y. Tao, X. Chen, G. Luo, P. Sun, C. Sun and D. Sun, *Angew. Chem., Int. Ed.*, 2023, **62**, e202302595.
21 Q. Tang, Y. Lee, D.-Y. Li, W. Choi, C. W. Liu, D. Lee and D.-e. Jiang, *J. Am. Chem. Soc.*, 2017, **139**, 9728–9736.
22 Y.-M. Wang, X.-C. Lin, K.-M. Mo, M. Xie, Y.-L. Huang, G.-H. Ning and D. Li, *Angew. Chem., Int. Ed.*, 2023, **62**, e202218369.
23 C. Dong, R.-W. Huang, A. Sagadevan, P. Yuan, L. Gutiérrez-Arzaluz, A. Ghosh, S. Nematulloev, B. Alamer, O. F. Mohammed, I. Hussain, M. Rueping and O. M. Bakr, *Angew. Chem., Int. Ed.*, 2023, **62**, e202307140.
24 Y. Liu, J. Yu, Y. Lun, Y. Wang, Y. Wang and S. Song, *Adv. Funct. Mater.*, 2023, 2304184.
25 G. V. Goeden and K. G. Caulton, *J. Am. Chem. Soc.*, 1981, **103**, 7354–7355.
26 S. A. Bezman, M. R. Churchill, J. A. Osborn and J. Wormald, *J. Am. Chem. Soc.*, 1971, **93**, 2063–2065.
27 M. T. Pirnot, Y. M. Wang and S. L. Buchwald, *Angew. Chem., Int. Ed.*, 2016, **55**, 48–57.
28 J.-X. Chen, J. F. Daeuble, D. M. Brestensky and J. M. Stryker, *Tetrahedron*, 2000, **56**, 2153–2166.
29 D. M. Brestensky, D. E. Huseland, C. McGettigan and J. M. Stryker, *Tetrahedron Lett.*, 1988, **29**, 3749–3752.
30 C. Zhang, Z. Wang, W.-D. Si, L. Wang, J.-M. Dou, Z.-Y. Gao, C.-H. Tung and D. Sun, *ACS Nano*, 2022, **16**, 9598–9607.
31 F. Li and Q. Tang, *J. Catal.*, 2020, **387**, 95–101.
32 S. Biswas, S. Das and Y. Negishi, *Nanoscale Horiz.*, 2023, **8**, 1509–1522.
33 A. K. Ghosh and M. Brindisi, *J. Med. Chem.*, 2015, **58**, 2895–2940.
34 A. Matošević and A. Bosak, *Arch. Ind. Hyg. Toxicol.*, 2020, **71**, 285–299.
35 J. Bariwal and E. Van der Eycken, *Chem. Soc. Rev.*, 2013, **42**, 9283–9303.
36 Y. N. Zheng, H. Zheng, T. Li and W. T. Wei, *ChemSusChem*, 2021, **14**, 5340–5358.
37 Z. H. Guan, H. Lei, M. Chen, Z. H. Ren, Y. Bai and Y. Y. Wang, *Adv. Synth. Catal.*, 2012, **354**, 489–496.
38 M. Usman, Z.-H. Ren, Y.-Y. Wang and Z.-H. Guan, *RSC Adv.*, 2016, **6**, 107542–107546.
39 A. J. Jordan, G. Lalic and J. P. Sadighi, *Chem. Rev.*, 2016, **116**, 8318–8372.
40 J. Sun, X. Yan, L. Wang, Z. Xie, G. Tian, L. Wang, A. He, S. Li, Q. Guo, C. Chaolumen, J. He and H. Shen, *Inorg. Chem.*, 2023, **62**, 9005–9013.
41 Y. Bao, X. Wu, B. Yin, X. Kang, Z. Lin, H. Deng, H. Yu, S. Jin, S. Chen and M. Zhu, *Chem. Sci.*, 2022, **13**, 14357–14365.
42 R. Jin, G. Li, S. Sharma, Y. Li and X. Du, *Chem. Rev.*, 2020, **121**, 567–648.

